Experiments in Fluids (2006) 41: 295–307
DOI 10.1007/s00348-006-0156-3

RESEARCH ARTICLE

David F. Hill · Brian D. Younkin

PIV measurements of flow in and around scour holes

Received: 18 November 2005 / Revised: 1 March 2006 / Accepted: 18 April 2006 / Published online: 19 May 2006

Abstract Two sets of experiments related to the scour of cohesionless sediment by planar turbulent jets are presented and discussed. The first set of experiments measures the growth of the scour hole and downstream dune as a function of time. Measurements reveal a bedform that is nearly self-similar and whose growth in time is governed by a power-law relationship. The bedform is well represented by three linear segments with slopes near the angle of repose of the sediment. The second set of experiments uses Particle Image Velocimetry to characterize the mean velocity field in the scour hole and above the dune. For this set of experiments, a series of successively larger roughened fixed-bed models was used in place of the mobile bed. The measurements reveal the presence of strong recirculation in the hole and an attached wall jet on the main slope. Discussion of the utility of the present fixed-bed measurements in estimating shear stress along the bed and related application to predictive modeling of hydraulic scour is provided. Discussion of the technical challenges of similar mobile-bed measurements is also given.

1 Introduction

Hydraulic scour of cohesionless and cohesive soils is a process of great significance to many natural and engineered flows. In the context of natural river flows, a quantitative understanding of scour is of value in terms of predicting channel migration and the supply of sediment to estuaries and deltas. With regard to engineering applications, practical concerns include the resuspension and transport of contaminated sediments and the failure of dams, levees, and bridges due to the undermining of foundations.

The challenges in understanding the processes controlling hydraulic scour and developing a reliable predictive capability are myriad. The fluid flow is generally unsteady and three-dimensional and the sediment characteristics are often polydisperse and cohesive. Most crucially, the fine details of the fluid flow and sediment response at the water-bed interface have traditionally been inaccessible to the researcher. In the words of Balachandar et al. (2000), describing the state of scour research:

> A comprehensive understanding of the scour mechanics remains elusive because of the complex nature of the process. The coupling between the shape of the eroded bed profile and the hydrodynamics characteristics of the jet flow increases the complexity...Most previous studies have been experimental in nature and any attempts to theoretically model the scouring process have been semi-empirical at best. Furthermore, many of the suggested relationships provide a wide range of scour prediction for similar flow conditions.

From an empirical point of view, the scour of cohesionless and cohesive soils by horizontal planar and circular fluid jets has been well-studied in the past (Chatterjee and Ghosh 1980; Rajaratnam 1981; Ali and Lim 1986; Chatterjee et al. 1994; Chiew and Lim 1996; Aderibigbe and Rajaratnam 1998; Hamill et al. 1999; Dey and Westrich 2003; Mazurek et al. 2003). A simple schematic is shown in Fig. 1. Beginning with a horizontal bed, the response of the bed to the jet-induced shear stresses is to develop a scour hole, whose depth and streamwise location are functions of time. The

Communicated by EiF-0269-2005.R1

D. F. Hill (✉) · B. D. Younkin
Department of Civil and Environmental Engineering,
The Pennsylvania State University, 212 Sackett Building,
University Park, PA 16802, USA
E-mail: dfh4@psu.edu
Tel.: +1-814-8637305
Fax: +1-814-8637304
E-mail: bdy105@psu.edu

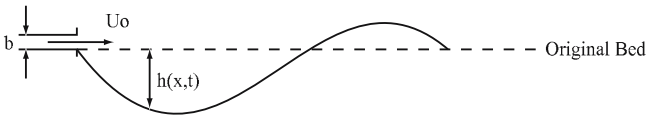

Fig. 1 Schematic of bed being eroded by horizontal turbulent jet

sediment scoured from the hole is deposited at a downstream distance where the shear stress is no longer sufficient for mobilization. Eventually, the hole deepens to the point where the scouring process is stopped. Note that some authors (Balachandar et al. 2000) have reported the *lack* of an equilibrium, even after multiple days of continuous scouring.

Complicating this scour process is the important influence of the tailwater depth, also referred to as the depth of submergence of the fluid jet. Previous studies (Johnston 1990; Aderibigbe and Rajaratnam 1998; Balachandar et al. 2000) have described two regimes, one where the jet is attached to the bed and another where the jet is attached to the free surface. In some experiments, the jet has remained within one of these regimes while in other experiments, the jet has been observed to oscillate or 'flick' between the two regimes. As will be discussed later, the present experiments fall within the bed jet regime due to the large tailwater depth used.

Most past experimental studies have sought to empirically correlate parameters such as maximum scour depth, maximum dune height, and the streamwise distances to the trough and dune with forcing parameters such as the jet velocity and height and sediment parameters such as the mean grain size and density. While of significant practical use, these studies have shed limited light on the underlying physics, thereby making extension to different parameter regimes difficult.

More recently, greater attention has been paid to measuring and simulating the properties of the flow field within scour holes themselves. For example, Kurniawan and Altinakar (2002) used an acoustic doppler profiler to measure the flow in a scour hole. Measurements were only made after equilibrium was reached, unfortunately, yielding no information about the development of the hole. Karim and Ali (2000) carried out some numerical simulations, using a variety of closure models, of the flow inside an equilibrium scour hole. The simulations showed good agreement with limited mean velocity measurements, but made no attempt to connect the flow to the scour process itself.

A significant conceptual step forward in connecting the flow to the erosion process itself was taken by Hogg et al. (1997). Their analysis began by incorporating existing empirical data on the mean velocity structure of wall jets. Next, the streamwise momentum equation was integrated in order to derive an expression for the boundary shear. By then making use of a criterion for incipient motion, the steady-state profile of the bed was derived and showed qualitative agreement with previous measurements.

The biggest obstacle to the work of Hogg et al. (1997) was the lack of existing data on boundary shear stresses on a mobile, evolving bed. In the absence of this data, their work made reasonable simplifying assumptions. By making use of classical (flat boundary) wall jet data, their analysis made the implicit assumption that the evolving boundary did not 'feed back' in the form of changes to the mean flow field. In an effort to heuristically correct for this, their analysis used an arbitrary shape factor in its expression for the streamwise variation of shear stress. A Gaussian profile was used, in light of the fact that, in their words, 'there is no available model or data to prescribe the variation of [the shape factor].'

The intent of the present work is to provide a uniquely high resolution look at the mean velocity field in and around developing scour holes. The data obtained in the current study should subsequently help to refine or validate the types of assumptions, regarding boundary shear, that were made by Hogg et al. (1997). In a broader context, it is hoped that the present work will foster additional experimental studies of scour flows.

The specific scope of the present study can be stated as follows. Particle image velocimetry (PIV) measurements have been made downstream of a planar jet, parallel to and flush with an initially flat bed. Following live-bed experiments, carried out to chart the evolution of a two-dimensional scour hole and associated downstream dune, a series of roughened fixed-bed models of the bedform geometry was constructed. These models spanned the range from the initially flat bed to a point near the end of the bedform evolution. For each model, large ensembles of PIV realizations were acquired at numerous locations and tiled together into 'mosaic' images spanning as much of the flow field as practical.

The restriction of the experiments to the simplistic conditions of two-dimensionality and cohesionless sediments is intentional and frames the present study as one that is primarily conceptual. Future extensions to three-dimensional flows, such as a circular jet, and graded cohesive sediments are possible and anticipated.

2 Experimental facilities

The experiments were carried out in a custom-built recirculating flume, illustrated in Fig. 2. Water was withdrawn from one end, passed through a 1 horsepower centrifugal pump, a valve, and a digital flowmeter, before being discharged at the other end through a gently tapered planar nozzle, shown in Fig. 3. The nozzle was constructed with a variety of flow-conditioning materials inside, such as coarse fibrous pads and a honeycomb straightener. The height of the nozzle at its exit, b, was 1 cm, which, combined with a maximum flowrate through the system of 140 lpm, placed an upper bound

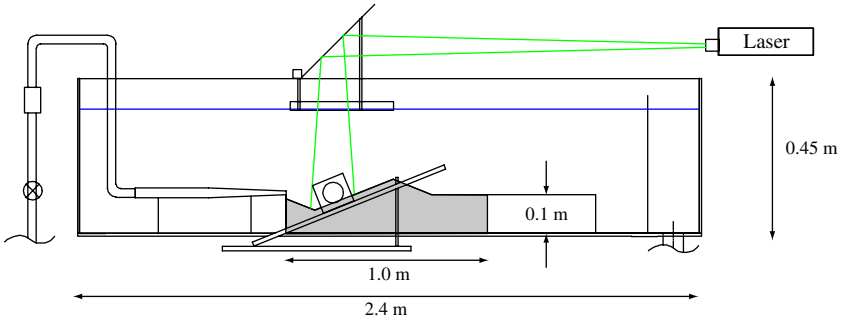

Fig. 2 Schematic of the experimental facility

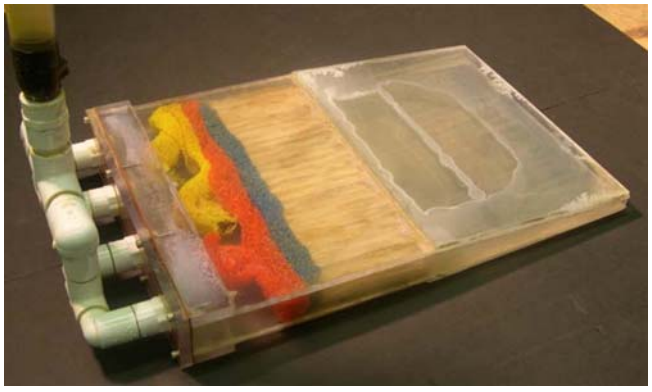

Fig. 3 Photograph of the planar nozzle

of approximately 7,800 on the Reynolds number of the exit flow.

Overall, the flume was 2.4 m in length, 30 cm in width, and 45 cm in height. A false floor was then constructed in order to create a cavity, or 'test section' immediately downstream of the nozzle. This cavity had a length of 1 m and a depth of 10 cm, with its upper edge flush with the bottom of the nozzle. For the live-bed experiments, the cavity was filled with sediment and for the PIV experimients, fixed-bed polycarbonate models were inserted into the opening, as is illustrated in Fig. 2. Separating the downstream end of the test section and the pump intake line was a trap, designed to minimize the amount of sediment passing through the pump. For all experimental trials, the free surface was maintained at an elevation of 25 cm above the jet axis.

For the first experimental phase, live-bed experiments were carried out with three sediment sizes. Glass beads (Ballotini Impact Beads, from Potters Industries), having a specific gravity of 2.5, were used instead of natural sediments. The decision to use artificial rather than natural sediments was consistent with the overall experimental goal of initially removing as much variability as possible. Planned future studies will address the effects of the irregularity in shape and the gradation found in natural sediments. The mean diameters d_{50}, calculations of settling velocity V_s, and measured angles of repose θ of the glass beads are summarized in Table 1 and a sample photograph of the 'B' glass beads is shown in Fig. 4. Note that the specific gravity of 2.5 is in close proximity to typical values ($\sim$ 2.65) for sandy sediments.

For the second experimental phase, PIV measurements were made with a PIV system from TSI, Inc. The system consisted of a four megapixel camera, double-pulsed (120 mJ/pulse) Nd:Yag lasers, a synchronizer to facilitate system timing, and frame grabbers to facilitate image acquisition. As shown in Fig. 2, an angled camera mount was used in order to align the camera with the main slope of the bedform model. The laser light sheet was introduced from above and a shallow glass 'pan' was used in conjunction with a deep tailwater in order to eliminate refractions from slight free surface disturbances.

As shown in Fig. 5, a series of fixed-bed models were constructed for this experimental phase. Made of polycarbonate and roughened with sediment grains painted a flat black, the series of models was chosen to span a wide range of the scour hole development. The use of fixed-bed models rather than a live bed was a compromise aimed at allowing for the acquisition of large ensembles of data. For each model, ensembles of 1,000 image pairs were obtained at numerous locations in the flow field. If a live bed were used, the bed would change noticeably in the amount of time that it took to fully image the flow field.

3 Live-bed experiments

3.1 Bedform geometry

Visual observations from initial tests revealed that the scour hole and downstream dune that were generated by the planar jet were highly two-dimensional in nature. As a result, it was determined that the shape of the bedform, at different instances in time, could adequately be determined by periodically stopping the

Table 1 Mean grain diameters, settling velocities, and angles of repose of the solid glass spheres used in the present experiments

Sediment	d_{50} (μm)	V_s (cm s^{-1})	θ (°)
A	725	14.2	23.3
B	513	10.3	22.2
AC	88	0.94	23.7

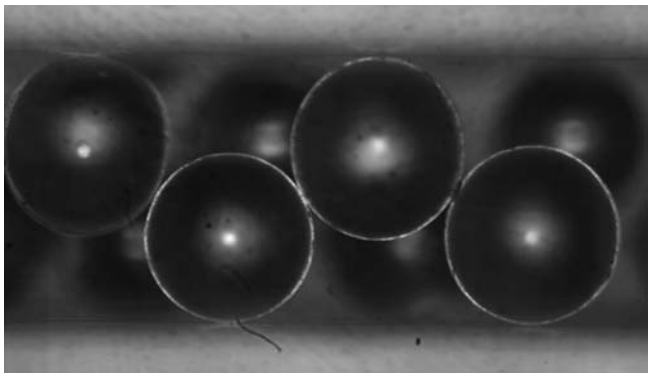

Fig. 4 Microscopic image of type B sediment in a 1 mm rectangular channel

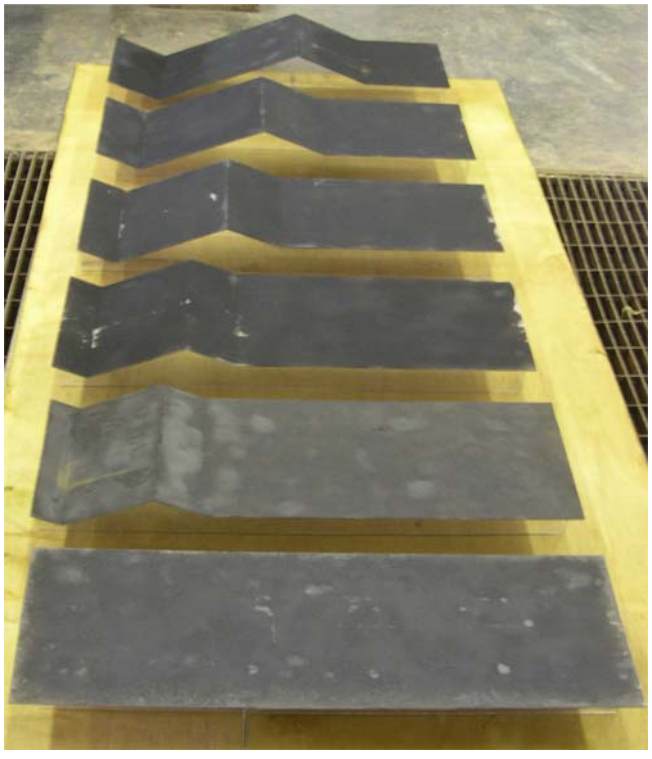

Fig. 5 Fixed-bed models constructed to represent various stages of development of the scour hole and downstream dune

pump and tracing the profile on the sidewall of the flume. As a representative example, Fig. 6 shows the bedform, determined in this manner, for the experiment with B sediment and a flowrate of 120 lpm. The profiles observed at the different times display a degree of self-similarity, particularly in the vicinity of the dune.

It should be noted that these profiles represent 'static' beds. Other authors (Aderibigbe and Rajaratnam 1998) have noted the difference between static and dynamic beds, a difference that increases with increasing particle densimetric Froude number

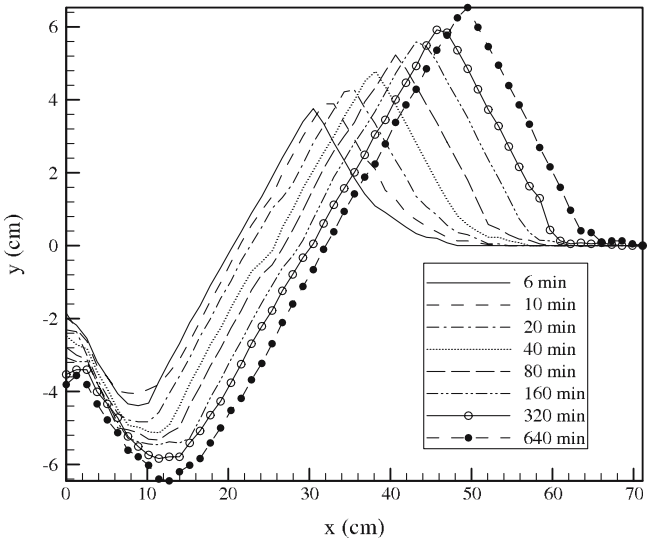

Fig. 6 Evolution of the dimensional bedform for the B120 experimental trial

$$F_0 = \frac{U_0}{\sqrt{g(\Delta\rho/\rho)d_{50}}}, \tag{1}$$

where U_0 is the initial jet velocity, $\Delta\rho$ the difference in density between the sediment and fluid and ρ the fluid density. Additionally, Johnston (1990) and Aderibigbe and Rajaratnam (1998) remark on the unsteady nature of the jet in their live-bed experiments, with the jet oscillating between a horizontal position and one where it is deflected down into the scour hole. To an extent, this behavior was observed in the present live-bed experiments, although not to the degree reported by Johnston (1990) and Aderibigbe and Rajaratnam (1998). This is due to the generally lower values of F_0 and the larger values of tailwater depth in the present experiments. Regardless, it should be acknowledged that the reliance of the present study upon static profiles has the effect of filtering out the unsteady nature of the bed entirely.

Scaling the bedforms by any characteristic length scale, say the distance to the crest, x_{crest}, confirms that the profiles are highly self-similar, with some minor discrepancies found in the trough and at the downstream edge of the dune. This is illustrated in Fig. 7, again for the case of B sediment with a flowrate of 120 lpm.

With an eye towards a simplistic model of bedform evolution, it was decided to parameterize the bed with as few parameters as possible. To this end, an attempt was made to represent the scaled bedform with three linear segments of equal/opposite slope and an offset, or intercept, at the origin. This model profile, along with the dimensionless B sediment bedform, averaged over all flow trials, ranging from 60 to 140 lpm, is shown in Fig. 8. Note that this two-dimensional model profile imposes conservation of sediment mass and that the slope and offset parameters were determined through

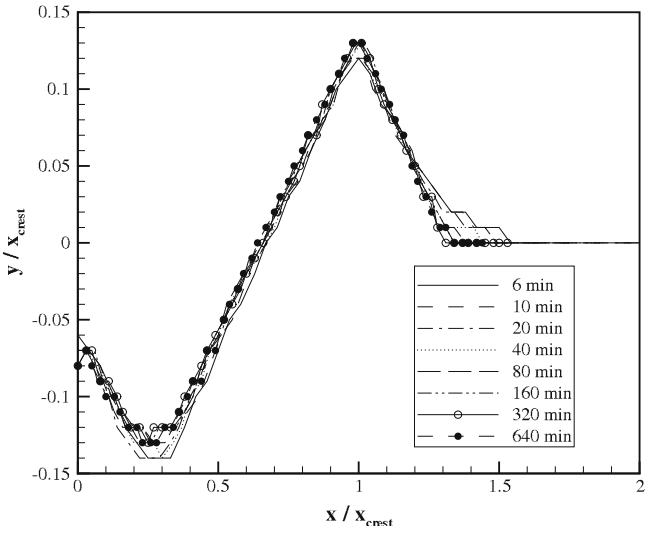

Fig. 7 Scaled bedforms for the B120 experimental trial

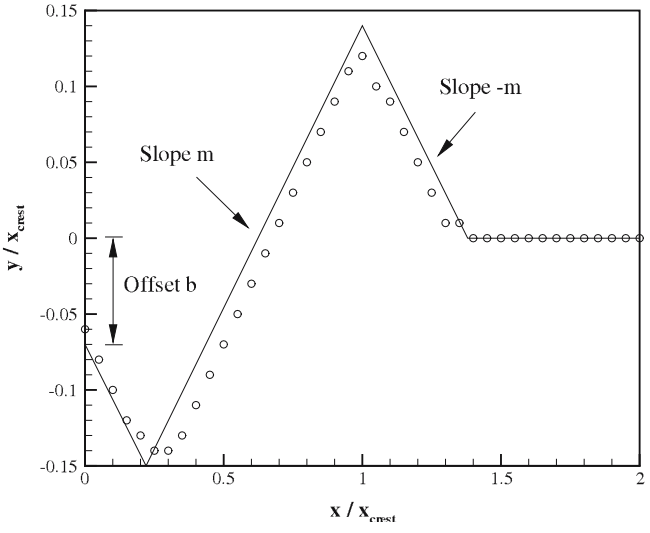

Fig. 8 Dimensionless bedform (*circle*) for the B sediment, averaged over all trials, along with linear approximation of the bedform

least-squares analysis. This linear approximation was subsequently used to construct the fixed-bed models described in Sect. 2 and shown in Fig. 5.

For the A and B sediments, the scaled profiles each yielded $m = 0.395$ and $b = 0.07$. The AC sediment, on the other hand, deviated significantly from this simple profile. This was due to the fact that the AC sediment was fine enough to be put into suspension by the fluid jet. As a result, the sediment was carried and deposited far downstream of the dune, unlike the A and B trials, where the sediment simply rolled over the crest of the dune. The scope of the present velocity measurements was limited to these latter cases, characterized by bedload transport.

It is clear from Fig. 8 that this model representation of the bed is not perfect, even for the bedload transport cases of the A and B sediment. The discrepancies suggest a lack of conservation of sediment in the experimental data. Recalling that bedform profiles were obtained at the sidewall only, a possible explanation is that slight three-dimensionality of the bedform was present. This hypothesis was tested for a single flow rate (100 lpm) for the A sediment. For this trial, bedform profiles were obtained at several times both at the sidewall and along the flume centerline. The latter measurements were carried out with a standard point gage, having a resolution of 0.025 mm.

Figure 9 shows these two profiles, scaled and averaged over the duration of the trial. They indicate that there is some degree of three-dimensionality, with the crest being slightly higher and the trough being slightly shallower on the flume centerline. This may be due to the interaction between the sidewall boundary layer and the lower free shear layer of the jet. As the jet discharges, spanwise vorticity is created above and below the jet axis. Near the flume sidewalls, the presence of a spanwise gradient in streamwise velocity results in streamwise vorticity being generated through the mechanism of vortex tilting. This streamwise vorticity, concentrated adjacent to the sidewalls, serves to 'mine' small amounts of sediment away from the walls, resulting in a slightly deeper trough at the sidewall than at the centerline. Given that the centerline measurements are far more time-intensive, however, than those at the sidewall, it was decided to use only the latter in determining the model bed as described above.

3.2 Scour rate

One final point of interest regarding the live-bed experiments is how the bedform evolves with time. From a dimensional analysis point of view, there are a great

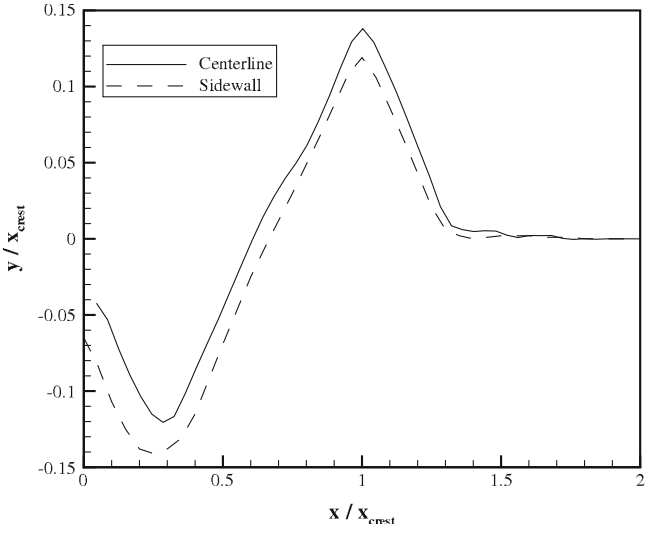

Fig. 9 Dimensionless bedforms for the A100 trial. Profiles are obtained from the flume sidewall and from the flume centerline

number of independent variables in the present problem and the literature is characterized by many different scalings. As many of these variables (e.g. nozzle thickness, tailwater depth, fluid and sediment densities, etc.) were not varied in the present experiments, they can be removed from the analysis. Moreover, if the assumption of fully turbulent flow is made and a single grain size is considered, a dimensional relationship such as

$$x_{\text{crest}} = f(U_0, g, t), \tag{2}$$

where U_0 is the initial jet velocity and g is gravity, may be proposed. This yields the equivalent dimensionless relationship

$$\frac{x_{\text{crest}}}{U_0 t} = f\left(\frac{gt}{U_0}\right). \tag{3}$$

Again, it is noted that other relationships are possible, depending upon the initial choice of parameters.

Figure 10 shows, as an example, the B data, plotted in this fashion, and on logarithmic axes. First, it is clear that the bedform evolution follows a power-law dependence, i.e.

$$\left(\frac{x_{\text{crest}}}{U_0 t}\right) = \alpha\left(\frac{gt}{U_0}\right)^{\beta}. \tag{4}$$

This indicates that, in a strict sense, the bedforms were not yet in an equilibrium state at the conclusion of each trial. Note that the trials ranged in duration from 4 to 20 h, depending upon the combination of sediment size and flow rate. The practical desire to perform a large set of trials precluded longer runs and individual trials were therefore terminated when bedload transport was observed to diminish to a minimal level. It is acknowledged that this termination point was a subjective measure.

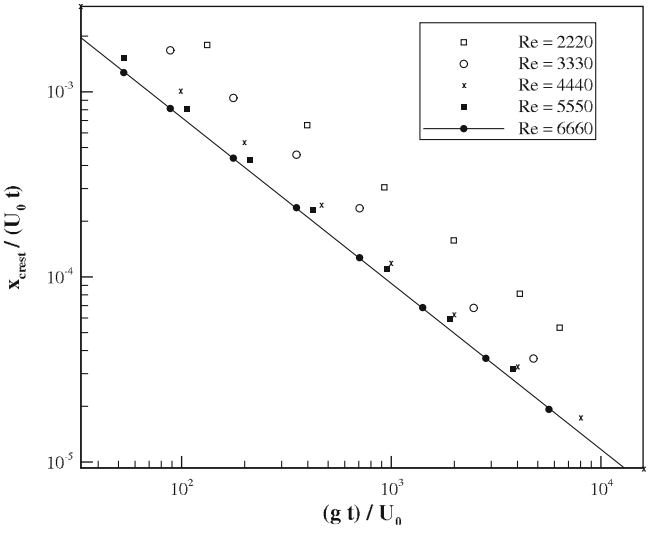

Fig. 10 Variation of dimensionless distance to crest with dimensionless time for B sediment experiments. The *solid line* is a power law fit to the highest Re trial

The Reynolds and densimetric Froude numbers, the obtained power-law coefficients, and the correlation coefficients of the power-law fits for the various trials are summarized in Table 2. Additionally, the power-law coefficients are plotted in the two-dimensional Re $-$ F_0 parameter space in Fig. 11.

Both Figs. 10 and 11 suggest that, with increasing Reynolds number, the data are approaching Reynolds number invariance. Additionally, the data indicate a clear variation with grain size. Finally, the values of β given in Table 2, in conjunction with (4), which indicates that the bedforms grow by $t^{1+\beta}$, reveal a growth coefficient of $\sim$0.05–0.15. Despite the depth of the literature on hydraulic scour, there appear to be only limited points of comparison. For example, Rajaratnam (1965, Fig. 2b) reports a coefficient of approximately 0.15 for a trial with $d_{50} = 1.2$ mm and $F_0 = O(10)$. Chatterjee et al. (1994) similarly give coefficients in the range of 0.15–0.20. Ali and Lim (1986) report a higher coefficient of 0.33, but it should be noted that their experiments had very shallow tailwater depths. It is possible that the lower coefficients being reported in the present study arise from the highly idealized artificial sediment that was utilized. Planned future trials with natural sediments may help to resolve this.

4 Velocity measurements

As discussed in the previous sections, a series of successively larger fixed-bed models was constructed out of polycarbonate. Given the appreciable data storage and processing requirements of the PIV measurements, it was decided to focus on a single sediment–flow rate combination. The A sediment and a flow rate of 140 lpm were chosen. Therefore, the sizes of the models were chosen to span the range from (initially) flat bed to the ultimate size recorded in the A140 live-bed experiment.

For each model, the camera was positioned at a number of locations so that the flow field in the vicinity of the bedform was fully covered, as illustrated in

Table 2 Summary of experimental trials and curve-fit parameters

Trial	Re	F_0	α	β	Correlation coefficient
AC40	2,222	6.18	3.71	−0.844	0.9994
AC60	3,333	9.26	2.97	−0.846	0.9982
AC80	4,444	12.35	2.33	−0.836	1.0000
AC100	5,555	15.44	2.14	−0.834	0.9999
B40	2,222	2.56	9.49	−0.904	1.0000
B60	3,333	3.84	11.7	−0.970	0.9998
B80	4,444	5.12	5.31	−0.929	1.0000
B100	5,555	6.39	3.53	−0.904	1.0000
B120	6,666	7.67	2.72	−0.894	1.0000
A60	3,333	3.23	10.07	−0.960	1.0000
A80	4,444	4.30	5.87	−0.939	1.0000
A100	5,555	5.38	5.05	−0.943	0.9999
A120	6,666	6.45	2.77	−0.907	0.9999
A140	7,777	7.53	2.17	−0.895	1.0000

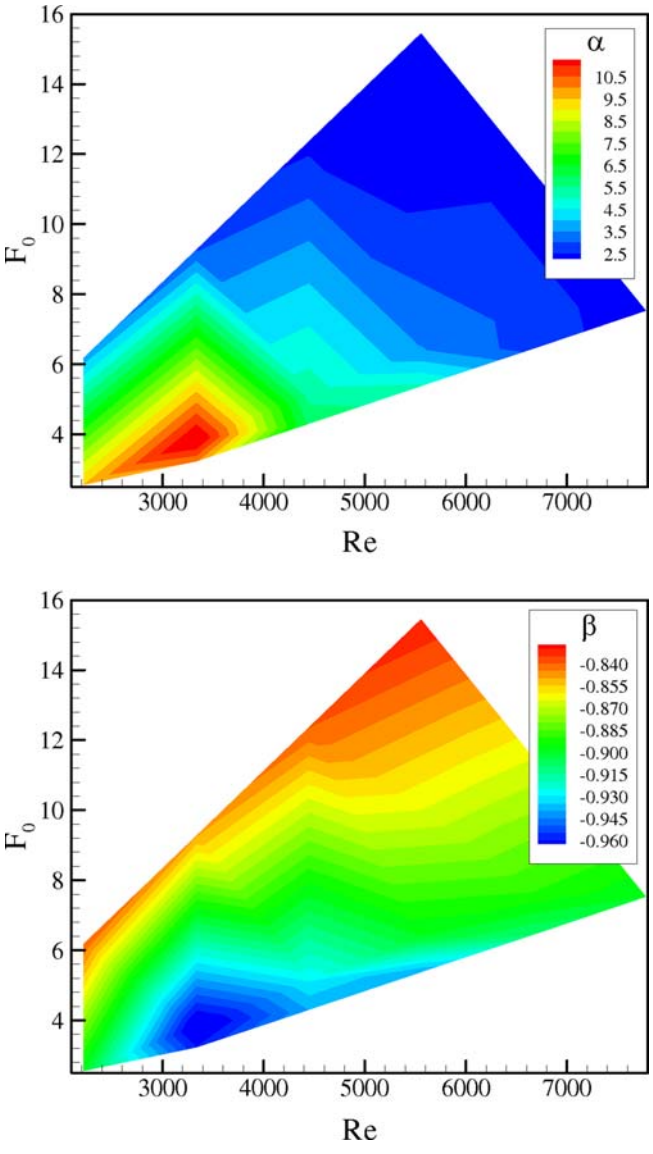

Fig. 11 Contours of power-law coefficients with Re and F_0

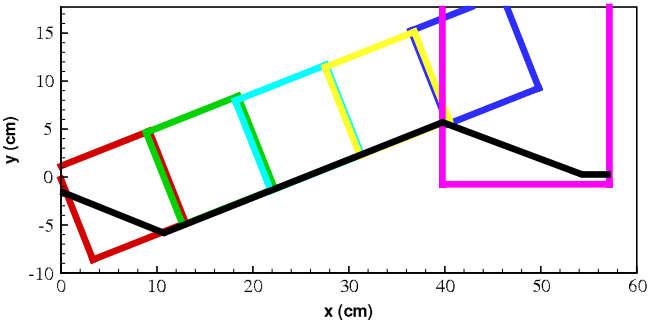

Fig. 12 Illustration of typical camera fields of view. The *solid black line* indicates the upper boundary of the fixed-bed model

Fig. 12. During post-processing, the individual fields of view were tiled together into a composite, or mosaic, image of the entire flow field. This was done by using calibration images for each field of view, each of which provided a unique mapping between raw pixels and dimensional position for that field of view in laboratory coordinates.

At each individual location, an ensemble of 1,000 image pairs was obtained. The storage requirement for the raw 12-bit images for the five models therefore amounted to $\sim$ 400 GB. The image pairs were subsequently interrogated with PIVSleuth (Christensen et al. 2000) and validated using CleanVec, both developed at the Laboratory for Turbulence and Complex Flow at the University of Illinois. Images were interrogated with 32×32 windows, using a 50% overlap. Typical vector removal rates ranged from 1 to 5%, with the bulk of removed vectors being near the bed or near the left and right edges of the images. In the case of the bed, moderate scattering of laser light from the sediment grains was responsible, despite efforts to minimize this with flat black paint.

With regards to measurement accuracy, some estimates are available from Raffel et al. (1998, Sect. 5.5). Their Monte Carlo simulations suggest that, for a 32×32 interrogation window and particle image diameters of 1–3 pixels, displacement uncertainty is around 0.02 – 0.04 pixels. For the present experiments, computed mean streamwise particle displacements were on the order of a few pixels, indicating that the uncertainty was similarly on the order of a few percent.

The mean velocity fields for the flat bed and the five model bedforms are given in Fig. 13. Both color contours of horizontal velocity and velocity vectors are provided. For the sake of visual clarity, only a very small percentage of the total velocity vectors are displayed. Casual observation of the mean velocity fields reveals several interesting and important aspects of the flow. First, recirculation of the flow is observed in the scour hole itself. This was observed in the live-bed experiments and this vortex played a significant role in the erosional process. Sediment would be swept in a clockwise fashion from the bottom of the scour hole up into the strong jet flow of the discharge, at which point it would be carried downstream.

A more detailed view of the vortex flow in the scour hole is provided in Fig. 14. In this closeup view of the mean velocity, the velocity components have been scaled by the initial jet velocity and the horizontal and vertical coordinates have been scaled by x_{crest}. As with Fig. 13, only selected vectors are shown for the sake of clarity. As the bedform progresses in scale from small to large (moving from Profile 1 to 5), the most interesting feature is that the vortex progressively moves closer to the leading edge of the bedform. As summarized in Table 3, noting that $x/x_{\mathrm{crest}} = 0.269$ corresponds to the nondimensional location of the model trough, the vortex resides on the main slope, i.e. between the trough and crest, of the bedform for the first two models. As the scour progresses to the latter three model sizes, the vortex moves toward the origin and resides on the slope between the jet orifice and the trough.

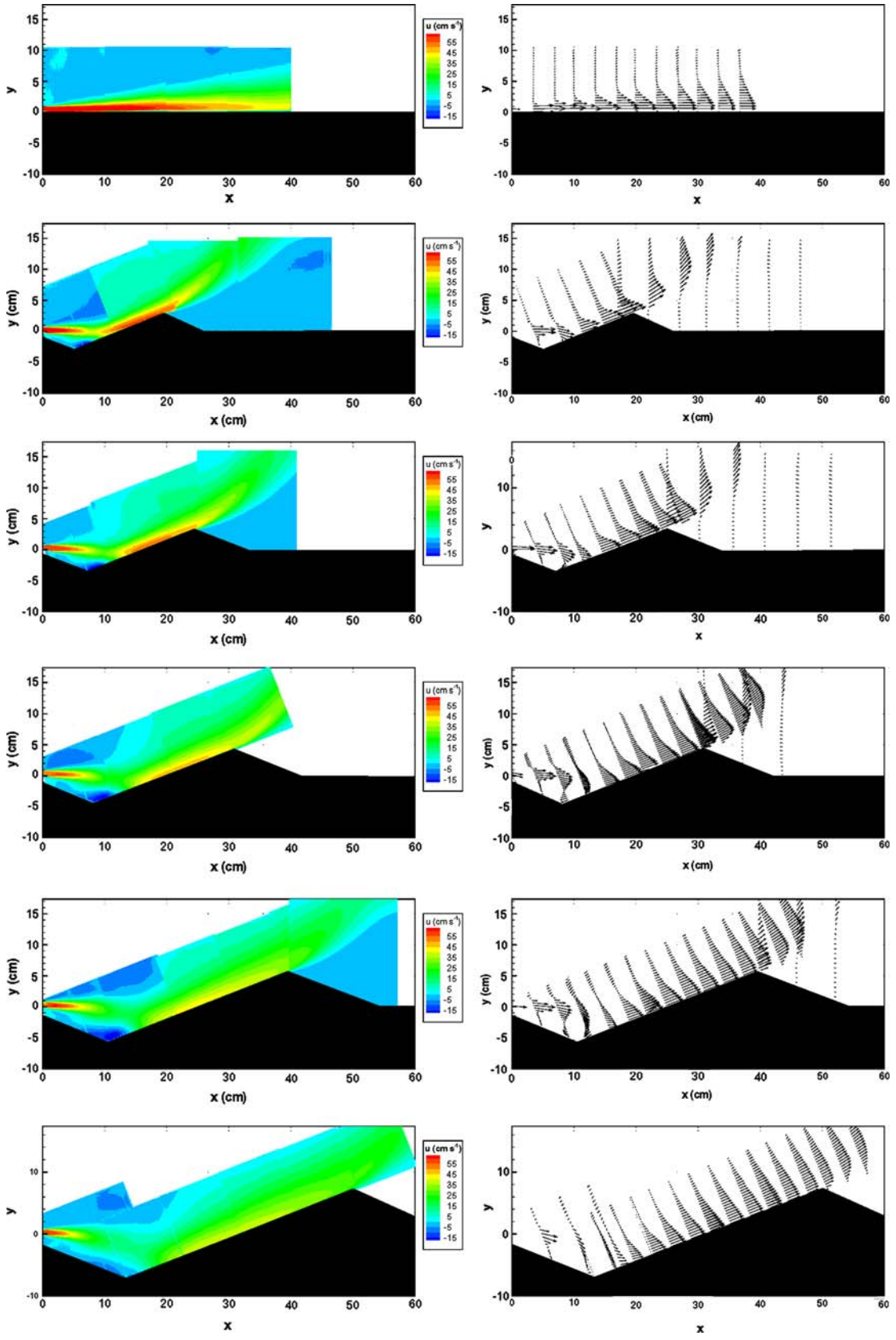

Fig. 13 Mean velocity fields for the fixed bed, A sediment, 140 lpm trials. *Color contours* denote horizontal velocity and only selected vectors are shown for clarity

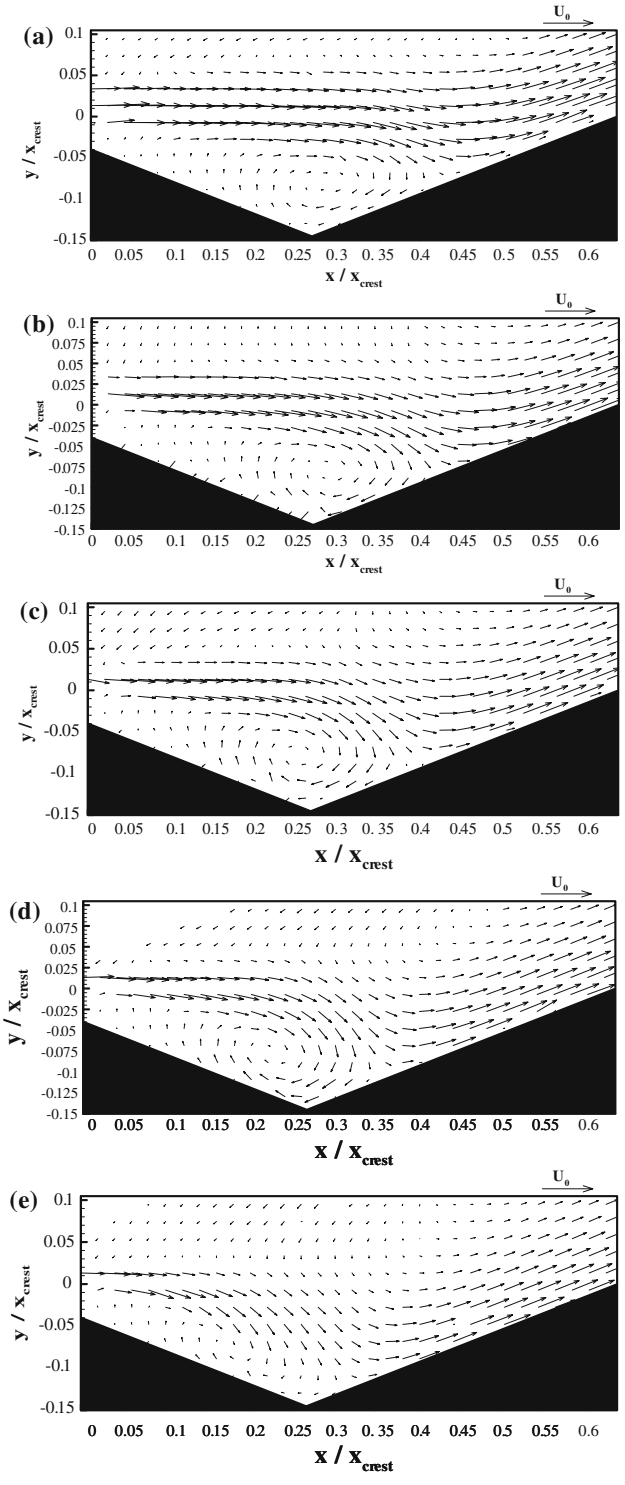

Fig. 14 Two-dimensional vector representation of mean velocity fields in the scour hole for the five fixed-bed models. **a** Through **e** correspond to Profiles 1 through 5, respectively

Next, very little flow is observed in the lee of the dune. The flow separates over the crest of the dune and only an extremely weak recirculation is observed. Recall that observations of the live-bed experiments revealed that sediment carried along the main slope simply rolled down the downstream side of the dune, which was essentially at the angle of repose of the sediment. Figure 15 shows scaled vertical profiles of streamwise velocity at streamwise locations of $x/x_{\text{crest}} = 1$ and 1.362. These locations corresponds to the crest itself and the downstream limit of the downstream slope of the crest where the bed returns to horizontal. As indicated in the figure, the magnitude of the return flow, i.e. that headed up the slope, is limited to approximately 5–10% of the initial jet velocity while the magnitude of the jet flow that separates off the crest of the dune and continues downstream can reach 50–75% of U_0.

Third, the main jet flow is seen to deflect downwards and then attach to the main slope. Subsequent to attachment, the flow appears to behave like a classic wall jet. In the context of the erosion of the bed, the velocity results help to understand the basic mechanisms at work. From the point of attachment of the jet on the main slope to the dune crest, sediment transport is driven by shear along the slope. For the A and B sediments, as discussed previously, this transport appeared to be largely bedload. Upstream of the point of attachment, sediment is mined out of the trough by the vortex, lifted into the flow exiting the nozzle, and swept downstream. As sediment passes over the crest of the dune, it essentially rolls down the slope, under the action of gravity. As the bedform increases in size, the attachment point moves further and further away from the jet orifice and the velocity shear along the main slope weakens. This leads to a gradual slowing and, presumably, eventual cessation of the scour. When the bedforms and the velocity results are considered in a scaled format, as in Fig. 14, it is interesting to note that, as was the case with the location of the trough vortex, the point of attachment of the jet on the slope migrates toward the jet origin as the bedform grows. Table 4 gives the location of the point of reattachment, x_r, in nondimensional terms.

4.1 Streamwise variation of maximum velocity

From the point of view of simple parameterizations of the flow, leading to modeling estimates of the erosion rate, the similarity of the flow on the main slope to classic wall jets will be further explored. Recall that Hogg et al. (1997) used established wall jet power law equations in deducing expressions for the variation of boundary shear. Figure 16 shows the variation of maximum velocity with distance from the jet orifice. The results in Fig. 16a are for the flat bed case. The maximum streamwise velocity component is normalized with the jet exit velocity U_0 and the streamwise distance is normalized with the initial jet thickness b. The plot is on log–log axes and the straight-line fit for the region downstream of $\sim 10\ b$ demonstrates the well-known power law decay of a wall jet. The observed decay coefficient of -0.43 is in good agreement with the results of Tachie et al. (2004) who report

Table 3 Nondimensional streamwise location of the trough vortex (x_v) for the different fixed-bed models

Profile	x_v/x_{crest}
1	0.285
2	0.283
3	0.254
4	0.227
5	0.175

−0.455 and who note little difference between rough and smooth boundaries.

Figure 16b shows similar results for the five model beds, with some slight differences in presentation. Instead of considering only the streamwise velocity component, the maximum magnitude of the velocity vector, i.e. $|\overline{U}|_{max}$ is plotted as a function of distance. This addresses the fact that the flow is no longer unidirectional, as was the case for the flat plate. Also, the streamwise coordinate is now normalized by x_{crest} so that the data from the different model sizes can be compared on a common axis.

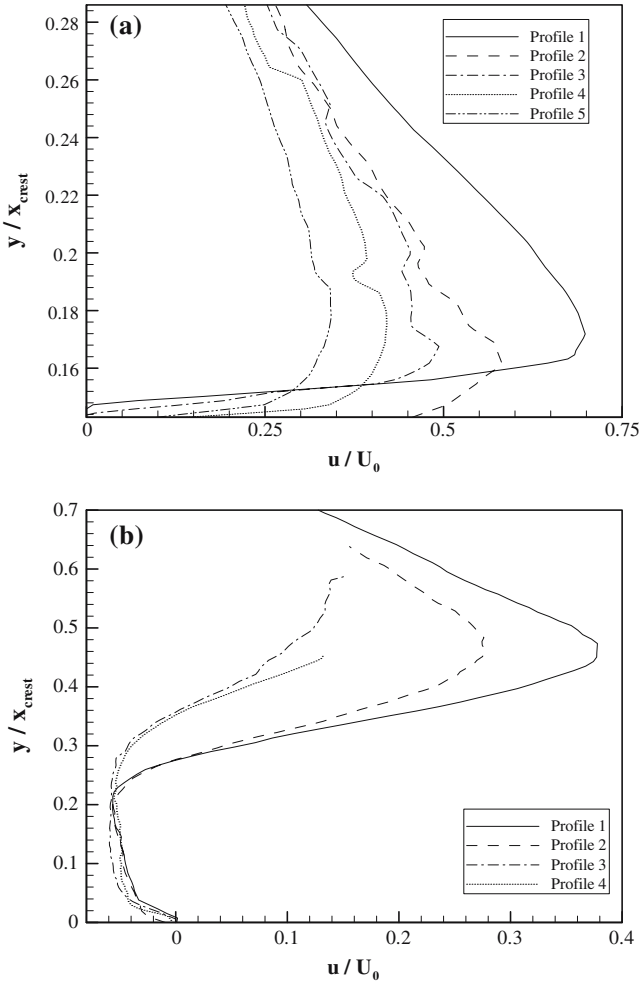

Fig. 15 Vertical profiles of streamwise velocity at **a** $x/x_{crest} = 1$ and **b** $x/x_{crest} = 1.362$

It is observed the streamwise variation in maximum velocity is far more complex for the flow over the model beds, although distinct regimes can be identified. Initially, in the range of $x/x_{crest} < 0.3$, the jet is basically a free jet and significant decay is observed. Note that, due to the choice of scaling of the x axis, the different curves do not appear to have similar slopes. Plotted against x/b instead, all five curves do indeed have similar slopes in this initial region. Note as well that the observed decay is somewhat unexpected. The downstream limit of this region ranges from about $5b$ for the smallest model to about $15b$ for the largest model. The development region of free and wall jets is generally at least this large (see Fig. 16a) and does not exhibit appreciable decay of maximum velocity. This suggests that perhaps the trough vortex plays a role in enhancing the observed initial decay of the jet.

Next, in the range of $0.3 < x/x_{crest} < 0.6$, the velocity increases as the jet attaches to and is accelerated along the slope. Third, in the range of $0.6 < x/x_{crest} < 1$, which corresponds to the region of the fully attached wall jet, the maximum velocity decays fairly weakly and not in a definitive power-law fashion. Finally, when $1 < x/x_{crest}$, the jet has separated off of the crest and decays rapidly with further downstream distance. This complex structure of the variation of maximum velocity with distance, in the case of the model beds, appears to limit the use of classic wall jet relations in determining boundary shear stress.

5 Boundary shear estimates

To return to one of the main motivations of this work, it is of interest, therefore, to determine whether or not boundary shear stress data can be extracted from high resolution PIV velocity data over bedform. This information will be of considerable interest and use, given the broad impact of sediment transport in natural and engineered environments. Generally speaking, there are many candidate methods for determining boundary shear.

In the case of a geometrically simple flow, such as uniform open channel flow, theoretical knowledge, obtained from the equations of motion, of the variation of stress can be used to extrapolate boundary shear from measurements made in the fluid interior. Alternatively, if a flow has been well studied, it is possible that well accepted equations for mean velocity profiles exist. These equations may include the shear velocity, allowing for the determination of boundary shear through fitting of experimental velocity data. As a third option, boundary shear can determined if velocity measurements in the viscous sublayer are available. For the present study, all of these methods appear to be unsatisfactory. Paying particular attention to the lattermost approach, rough estimates sug-

Table 4 Nondimensional streamwise location of jet reattachment

Profile	x_r/x_{crest}
1	0.425
2	0.423
3	0.390
4	0.359
5	0.319

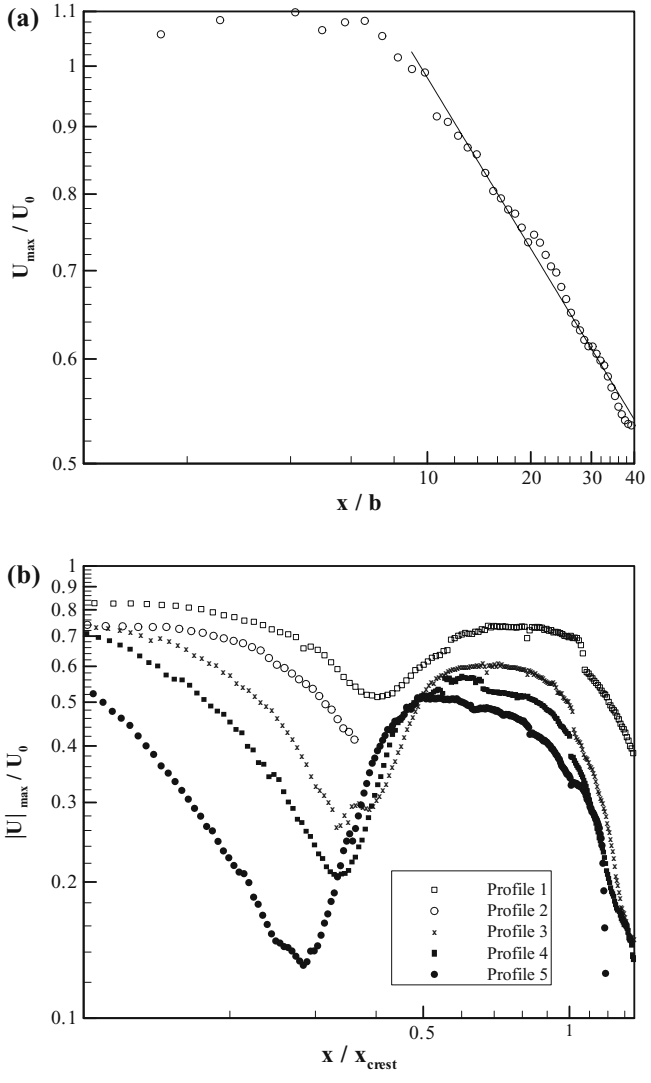

Fig. 16 **a** Variation of maximum streamwise velocity with distance along the flat plate. The *trendline* indicates a power-law fit to the data. **b** Variation of maximum velocity vector magnitude with scaled streamwise distance. *Profiles 1* through *5* denote the smallest to the largest model beds

gest that the sublayer should be on the order of a few tenths of a millimeter. Despite efforts to minimize scattering of laser light by the bed, reflections were sufficiently bright in practice so as to prevent measurements this close to the boundary. One possibility for future studies is to use particles (such as PTFE) that have a refractive index very close to water and use refractive matching techniques to adjust the index of the water to that of the PTFE.

An option that remains is using a quadratic friction law to estimate the boundary shear based upon the mean velocity data. As discussed in numerous papers on wall-bounded shear flows from the very early (Rajaratnam 1965) to the very recent (Tachie et al. 2004), the boundary shear τ_0 may be expressed as

$$\tau_0 = \frac{1}{2} c_f \rho u_m^2, \tag{5}$$

where ρ is the fluid density, u_m is the maximum streamwise velocity at a given streamwise location, and c_f is a friction coefficient. Studies such as Rajaratnam (1965) provide experimental data on the variation of c_f with local Reynolds number for smooth boundaries. Tachie et al. (2004) pay specific attention to the case of rough boundaries and their data indicate that c_f is fairly independent of Reynolds number and has a value of roughly 0.008.

Using the above information, the boundary shear stress was determined for each of the five model bedforms. Figure 17 shows the variation of stress with a normalized alongslope distance, x'. Here, a value of 0 corresponds to the trough and a value of 1 to the crest. The maximum velocity u_m corresponds to the maximum alongslope velocity found by scanning in the slope-normal direction at different values of x'. Results are only given for the range 0.5–1, which roughly corresponds to the portion of the slope where the jet is attached.

The results confirm that, as the scour hole gets larger, the shear along the slope, which is driving the sediment transport, weakens. Additionally, it is seen that the variation in boundary shear along any given slope is only moderate.

As a rough check on the results, note that the Shields parameter for incipient sediment motion is defined as

$$\tau_c^* = \frac{\tau_c}{(\gamma_s - \gamma)d}, \tag{6}$$

where τ_c is the critical bed stress required for motion, γ_s and γ are the specific weights of the sediment and fluid, and d is the grain size. This parameter has been shown to be a function of a Reynolds number based upon shear velocity and grain size, Re^*.

In the transitional regime, roughly $1 < Re^* < 70$, the relationship between τ_c^* and Re^* is given by the empirical fit (Yalin and Karahan 1979)

$$\tau_c^* = \sum_{i=0}^{4} A_i (\log Re^*)^i, \tag{7}$$

where $A_0 = 0.10000$, $A_1 = -0.13610$, $A_2 = 0.05977$, $A_3 = 0.01984$, and $A_5 = -0.01134$. Thus, for a given grain size and fluid and sediment densities, the critical stress is readily determined. For the A sediment used in the

roughened fixed-bed trials, a critical stress of 0.35 Pa is obtained. The nondimensional Shields parameter, the dimensional critical shear stress, and the critical grain size Reynolds number for the three sediment sizes are summarized in Table 5.

Next, it must be noted that this critical stress is relevant only to the case of a flat bed. Chiew and Parker (1994) report on experiments conducted with non-horizontal beds and express the ratio of critical shear on a non-horizontal bed ($\tau_{c_{nh}}$) to that on a horizontal bed (τ_{c_h}) as

$$\frac{\tau_{c_{nh}}}{\tau_{c_h}} = \cos\phi\left(1 - \frac{\tan\phi}{\tan\theta}\right), \tag{8}$$

where ϕ is the bed angle and θ the sediment angle of repose. For the present experiments, $\phi = -21.5°$ (negative since adverse), which leads to $\tau_{c_{nh}} = 1.78\tau_{c_h} = 0.62$ Pa.

From an idealized conceptual point of view, the fluid jet in a live-bed experiment strikes the slope someplace slightly upstream of the midpoint between the trough and crest. Sediment is dislodged and swept up the slope as bedload transport. As long as the shear stress at the point of jet impingement on the boundary exceeds the critical value required for motion, the scouring process will proceed. As the bedform grows, the point of impingement moves further away from the jet origin and the shear stress along the slope steadily declines. Eventually, the maximum shear along the boundary will fall below the critical value and the scouring process should cease. As Fig. 17 shows, the maximum shear along the slope of Profile 5, which represents a near-equilibrium state, is approximately 0.6 Pa. Given the large error bars typically associated with incipient motion criteria, this appears to be in reasonable agreement with the above calculations.

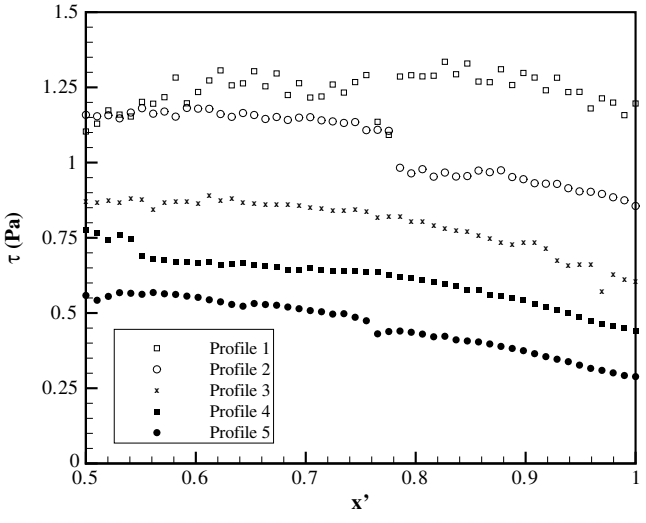

Fig. 17 Variation of boundary shear with normalized alongslope distance

6 Concluding remarks

The present study was undertaken in order to investigate the application of PIV to hydraulic scour problems. The main objectives were twofold: to obtain high-resolution images of the flow field within scour holes and above their associated dunes, and to use the velocity data to estimate the shear stress along the boundary. To assist in the execution of the study, several simplifying compromises were made. First, artificial cohesionless sediment, in the form of solid glass spheres, was used. Second, and based upon live-bed experiments, roughened fixed-bed models of the two-dimensional scour hole geometry were used during the PIV measurements. This ensured that the bed would not change during the amount of time that it took to image the entire domain.

The velocity data illuminated the recirculating flow in the scour hole and the nature of the jet flow as it emerges from the nozzle and eventually attaches to the sloping bed. While slope-normal profiles of alongstope velocity resemble a classic wall jet, it was found that the streamwise variation of maximum velocity was quite complex in structure. Due to the complexity of the flow and the measurements, the options for determining boundary shear stress from the velocity data appear to be limited. The use of a quadratic friction law illustrated the weakening boundary shear as the bedform progressed in size. Additionally, the predicted values of shear for the largest bedform, which represents the stage at which bedform evolution had nearly stopped, were in reasonable agreement with standard incipient-motion criteria.

The authors conclude that PIV measurements have a valuable role to play in sediment transport research. In the future, the use of either artificial sediment, close in refractive index to water, or fluorescent PIV seed particles and camera filters will improve the ability of the PIV measurements to resolve the flow details very close to the bed. Additionally, steady improvements in camera data transfer rates will result in the time scale of image acquisition becoming much less than the time scale of bed evolution. As a result, PIV measurements with live beds, particularly at the early stages of scour hole evolution, will become increasingly more feasible.

Table 5 Summary of incipient motion parameters for the studied sediments

Sediment	τ_c^*	τ_c (Pa)	Re^*
A	0.0326	0.349	13.5
B	0.0328	0.248	8.10
AC	0.100	0.129	1.00

References

Aderibigbe O, Rajaratnam N (1998) Effect of sediment gradation on erosion by plane turbulent wall jets. J Hydraul Eng 124(10):1034–1042

Ali K, Lim S (1986) Local scour caused by submerged wall jets. In: Proceedings of Instn. Civil Engineers 81:607–645

Balachandar R, Kells J, Thiessen R (2000) The effect of tailwater depth on the dynamics of local scour. Can J Civil Eng 27:138–150

Chatterjee S, Ghosh S (1980) Submerged horizontal jet over erodible bed. J Hydraul Div 11:1765–1782

Chatterjee S, Ghosh S, Chatterjee M (1994) Local scour due to submerged horizontal jet. J Hydraul Eng 120(8):973–992

Chiew YM, Lim SY (1996) Local scour by a deeply submerged horizontal circular jet. J Hydraul Eng 122(9):529–532

Chiew Y, Parker G (1994) Incipient sediment motion on non-horizontal slopes. J Hydraul Res 32(5):649–660

Christensen K, Soloff S, Adrian R (2000) PIV Sleuth—integrated acquisition, interrogation, and validation software for particle image velocimetry. Tech. Rep. 943, University of Illinois, Department of Theoretical and Applied Mechanics

Dey S, Westrich B (2003) Hydraulics of submerged jet subject to change in cohesive bed geometry. J Hydraul Eng 129(1):44–53

Hamill G, Johnston H, Stewart D (1999) Propeller wash scour near quay walls. J Waterw Port Coast Ocean Eng 125(4):170–175

Hogg A, Huppert H, Dade W (1997) Erosion by planar turbulent wall jets. J Fluid Mech 338:317–340

Johnston A (1990) Scourhole development in shallow tailwater. J Hydraul Res 28(3):341–354

Karim O, Ali K (2000) Prediction of flow patterns in local scour holes caused by turbulent water jets. J Hydraul Res 38(4):279–287

Kurniawan A, Altinakar M (2002) Velocity and turbulence measurements in a scour hole using an acoustic doppler velocity profiler. In: Proceedings of the third international symposium on ultrasonic Doppler methods for fluid mechanics and fluid engineering, Lausanne, Switzerland, pp 37–43

Mazurek K, Rajaratnam N, Sego D (2003) Scour of a cohesive soil by submerged plane turbulent wall jets. J Hydraul Res 41(2):195–206

Raffel M, Willert C, Kompenhans J (1998) Particle image velocimetry. Springer, Berlin Heidelberg New York, Sect. 5.5

Rajaratnam N (1965) The hydraulic jump as a wall jet. J Hydraul Div 91(5):663–673

Rajaratnam N (1981) Erosion by plane turbulent jets. J Hydraul Res 19:339–358

Tachie M, Balachandar R, Bergstrom D (2004) Roughness effects on turbulent plane wall jets in an open channel. Exp Fluids 37:281–292

Yalin M, Karahan E (1979) Inception of sediment transport. ASCE J Hydraul Div 105(11):1433–1443